

Long-term attitude dynamics of space debris in Sun-synchronous orbits: Cassini cycles and chaotic stabilization

S. Efimov¹ · D. Pritykin^{1,2} · V. Sidorenko^{1,3}

Received: 21 December 2017 / Revised: 19 June 2018 / Accepted: 27 August 2018 /

Published online: 19 September 2018

© Springer Nature B.V. 2018

Abstract

Comprehensive analysis of space debris rotational dynamics is vital for active debris removal missions that require physical capture or detumbling of a target. We study the attitude motion of large space debris objects that admittedly pose an immediate danger to space operations in low Earth orbits. Particularly, we focus on Sun-synchronous orbits (SSO) with altitude range 600–800 km, where the density of space debris is maximal. Our mathematical model takes into account the gravity-gradient torque and the torque due to eddy currents induced by the interaction of conductive materials with the geomagnetic field. Using perturbation techniques and numerical methods, we examine the deceleration of the initial fast rotation and the subsequent transition to a relative equilibrium with respect to the local vertical. A better understanding of the latter phase is achieved owing to a more accurate model of the eddy-current torque than in most prior research. We show that SSO precession is also a crucial factor influencing the motion properties. One of its effects is manifested at the deceleration stage as oscillations of the angular momentum vector about the direction to the south celestial pole.

Keywords Space debris · Attitude dynamics · Eddy-current torque · Cassini cycles

This article is part of the topical collection on Innovative methods for space threats: from their dynamics to interplanetary missions.

Guest Editors: Giovanni Federico Gronchi, Ugo Locatelli, Giuseppe Pucacco and Alessandra Celletti.

✉ S. Efimov
efimov.ss@phystech.edu

¹ Moscow Institute of Physics and Technology, 9 Institutskiy per., Dolgoprudny, Moscow Region, Russian Federation 141701

² Skolkovo Institute of Science and Technology, Nobelya Ulitsa 3, Moscow, Russian Federation 121205

³ Keldysh Institute of Applied Mathematics, Russian Academy of Sciences, Miusskaya Sq., 4, Moscow, Russian Federation 125047

1 Introduction

This paper presents a study of rotational dynamics of large space debris objects in Sun-synchronous orbits. SSO are characterized by 600–800 km altitude and inclination of about 98° (Vallado 2007). These orbits are best suited for the Earth observation from space, because of consistent lighting conditions in their subsatellite points for all satellite passes. Extensive use of SSO in the last few decades has led to accumulation of a vast space debris population in the region, a population that is beginning to pose a real threat to space activities. At present, the SSO region is characterized by the highest debris density and requires to be cleaned (Anselmo and Pardini 2016). Different aspects of active debris removal (ADR) missions are brought up in Bonnal et al. (2013) and Van der Pas (2014). One of the generally accepted ADR scenarios is tugging debris objects to the lower orbits, whereupon they burn in the atmosphere or fall to the Earth (Aslanov and Yudintsev 2013). Most ADR techniques are substantially influenced by debris object's rotational dynamics; hence, much effort has been spent lately to determine the rotation parameters through ground-based observations (Koshkin et al. 2016; Kucharski et al. 2014; Lemmens et al. 2013; Šilha et al. 2018; Santoni et al. 2013; Yanagisawa and Kurosaki 2012). At the same time, much attention has been paid to study the debris attitude dynamics theoretically (Gomez and Walker 2015; Lin and Zhao 2015; Ojakangas et al. 2012; Praly et al. 2012; Albuja et al. 2015; Sagnieres and Sharf 2017).

According to observation data (Šilha et al. 2018), there are two major types of large debris objects—defunct satellites and rocket bodies. Although much of what is discussed in this paper regarding the long-term attitude motion evolution is applicable to both classes of debris objects, there are also distinctions, which require separate treatment, e.g., taking into account the effects of Solar radiation pressure (Kucharski et al. 2014) or residual magnetic moment (Efimov et al. 2017b). For this reason, we shall here confine ourselves to the dynamics of the rocket bodies.

Rotational dynamics simulations for a typical object of the rocket-body class (Ariane 4 H10 stage) are conducted in Praly et al. (2012). The model we use in our study comprises the same key factors as in Praly et al. (2012) and Gomez and Walker (2015)—gravity-gradient torque and the torque due to eddy currents. We also take into account the orbit precession [cf. Lin and Zhao (2015)] responsible for remarkable dynamical effects unexamined in previous studies. Besides, when calculating the eddy-current torque, we employ a more accurate formula proposed in Golubkov (1972) and Martynenko (1985), which includes terms describing the influence of orbital motion that are considered small for fast rotations and are often neglected.¹ The fact that rotational dynamics at 500–1000 km altitudes is substantially influenced by torques due to eddy currents became clear immediately after the first artificial Earth satellites launches (Smith 1964; Ormsby 1967). It so happened, however, that when dealing with this phenomenon many researchers were mainly interested in fast rotations, whose orbital period is significantly greater than the rotation period. The complete formula for eddy-current torque allows correct description of all stages of the rotational dynamics evolution, including the one when the angular velocity is comparable to the mean motion. Moreover, it turns out that even for relatively large angular velocities (10–50 times greater than the mean motion) these terms can cause significant changes in the rotational axis direction for prograde spins. As in prior research, we neglect other environmental torques, which is acceptable for the chosen class of objects.

¹ Recently, Visco and Lucchesi (2018) presented an improved formula to calculate the eddy-current torque acting on satellites LAGEOS and LARES. However, it substantially relies on the spherical symmetry of those satellites, and thus it is unclear to what extent this approach can be applied to study the dynamics of other objects.

The attitude motion evolution can be divided into three stages (Efimov et al. 2017a): the *transient* stage, in which an arbitrary initial rotation is transformed into the rotation about the axis with the greatest moment of inertia (so called *flat rotation* or *principal axis rotation*), *exponential deceleration* of angular velocity, and the stage of *chaotic stabilization*. During the first relatively brief stage, the motion is primarily determined by internal dissipation. In the second stage, angular velocity decreases exponentially because of the eddy-current torque. When the angular velocity becomes comparable to the mean motion, the attitude dynamics appears to become chaotic. This chaos, however, is temporary in the case of rocket-body dynamics. It is usually followed by a regular regime with the object remaining nearly aligned with the local vertical. (More exactly, the final regime corresponds to small oscillations about the relative equilibrium.)

Analysis of space debris rotational motion in the stage of exponential deceleration can be carried out by perturbation techniques. Methodologically, this is the case of a rotating rigid body under the action of small conservative perturbations (the gravity-gradient torque and the influence of the orbit precession) and even smaller non-conservative perturbation (the eddy-current torque). Specialists, encountering similar situation in the studies of tidal evolution of celestial bodies' spin states (where tidal torque is also much smaller than the gravity-gradient torque), usually start from the consideration of effects caused by conservative perturbations and then establish how these effects are modified by smaller non-conservative perturbations (Gladman et al. 1966; Ward 1975). One particularly effective strategy is to consider the first integrals of a purely conservative model and reveal the variations of these quantities caused by the minute non-conservative factors. Then, relying on the relationship between the properties of the motions and values of the first integrals in conservative model, it is possible, *mutatis mutandis*, to describe qualitatively the evolution of the system's behavior over long time intervals. This is the approach that we shall adopt. One may also note that the analogy between secular effects due to the tidal torques and the eddy-current torques was indicated by Martynenko (1985).

The paper is organized as follows. Section 2 describes the main assumptions of our model and the equations for gravity-gradient torque and torque due to eddy currents. Section 3 presents the analytical study of the debris objects attitude motion evolution. We derive the evolution equations and interpret their solutions geometrically in terms of angular momentum direction. At the end of this section, we also provide the classification of the long-term evolution scenarios. Section 4 contains the simulation results validating the conclusions drawn from the analytical study and providing an understanding of the system's behavior in the stage of chaotic stabilization. Finally, the last section summarizes the results obtained for the characteristic evolution of large debris object rotational dynamics in SSO.

2 Mathematical model of a debris object rotational dynamics in SSO

Let us consider an object in a circular geocentric orbit of radius R_O and inclination i . The Earth's oblateness causes the orbit's precession with angular velocity

$$n_\Omega \approx -\frac{3J_2\mu_G^{1/2}R_E^2}{2R_O^{7/2}} \cos i,$$

where $R_E = 6378.245$ km is the Earth's mean equatorial radius, $\mu_G = 3.986 \times 10^5$ km³/s² is the gravitational parameter of the Earth, $J_2 = 1.082626 \times 10^{-3}$ is the first zonal harmonic

coefficient in the expansion of the Earth's gravity field. Our model pertains to SSO, where $\cos i < 0$ and, consequently, $n_\Omega > 0$, i.e., the longitude of ascending node increases.

Argument of latitude u varies as a linear function of time:

$$\dot{u} = \omega_D,$$

where $\omega_D = 2\pi/T_D$, T_D is the draconic period of the object's revolution around the Earth (the time between two consecutive passages through the ascending node). Employing the formula for draconic period, given in Vallado (2007), we obtain:

$$\omega_D = \omega_o \left[1 - \frac{3}{2} J_2 \left(\frac{R_E}{R_O} \right)^2 (1 - 4\cos^2 i) \right], \quad (1)$$

where ω_o is the mean motion for the circular orbit of radius R_O in the central gravity field with parameter μ_G .

As in prior research (Gomez and Walker 2015; Lin and Zhao 2015; Praly et al. 2012) when modeling the rotational dynamics with respect to object's center of mass, we shall take into account gravity-gradient torque \mathbf{M}_G and torque due to eddy currents \mathbf{M}_{EC} .

Gravity-gradient torque acting on the object in the Earth's gravity field is given by the formula (Beletsky 1966):

$$\mathbf{M}_G = \frac{3\mu_G}{R_O^5} \mathbf{R}_O \times \mathbf{J} \mathbf{R}_O, \quad (2)$$

where \mathbf{J} is the inertia tensor of the object and \mathbf{R}_O is the vector from the center of the Earth to the object's center of mass O .

Torque due to eddy currents can be expressed as (Golubkov 1972; Martynenko 1985):

$$\mathbf{M}_{EC} = -\mathbf{B} \times \mathbf{S}(\boldsymbol{\omega} \times \mathbf{B} - \dot{\mathbf{B}}), \quad (3)$$

where \mathbf{S} is the magnetic tensor of the object, $\boldsymbol{\omega}$ is the object's absolute angular velocity, \mathbf{B} is the magnetic field, the derivative $\dot{\mathbf{B}}$ is calculated in a non-rotating reference frame with the origin at point O . It is the $\dot{\mathbf{B}}$ term that makes Eq. (3) different from the simplified formula typically used in the studies of fast rotations.

The most accurate models of the geomagnetic field are provided by Working Group V-MOD, formed by the International Association of Geomagnetism and Aeronomy (IAGA). Analysis of the models, presented on the website of the Working Group (IAGA 2014), reveals that the dipole components account for 90% of the Earth magnetic field. It allows approximating geomagnetic field for astrodynamical applications by a field of a dipole placed into the center of the Earth (Hughes 2004):

$$\mathbf{B} = \frac{\mu_0 \mu_E}{4\pi R_O^3} \left[\frac{3\mathbf{R}_O(\mathbf{k}_E, \mathbf{R}_O)}{R_O^2} - \mathbf{k}_E \right],$$

where $\mu_0 = 4\pi \times 10^{-7} \approx 1.257 \times 10^{-6} \text{ N A}^{-2}$ is the magnetic constant, $\mu_E \approx 7.94 \times 10^{22} \text{ A m}^2$ is the Earth's magnetic dipole moment, \mathbf{k}_E is the dipole direction.

In Sect. 3, where the evolution equations are derived, we assume for simplicity that the dipole is directed along the Earth's rotation axis ("axial" dipole model). In Sect. 4, we validate this assumption by carrying out simulations with the use of a more precise model ("tilted" dipole, making an angle $\delta_\mu = 11^\circ 33'$ with the Earth's rotation axis). It is shown in Sect. 4.2 that within the accuracy of the averaging procedure the dipole model simplification is valid and allows studying the secular effects in the object's motion with the use of the evolution equations obtained for the axial dipole model.

2.1 Parameters

For all simulations and numerical estimates, we shall use a circular orbit with altitude $H = R_O - R_E = 770$ km and inclination $i = 98.7^\circ$. The initial motion is assumed to be a rotation about the axis with the greatest moment of inertia. That is to say, we omit from our study the first transient stage and start directly from the flat rotation regime, which usually sets in quite fast under the influence of internal dissipation due to the motion of residual fuel in the rocket-body fuel tanks (Ojakangas et al. 2012; Efimov et al. 2017a).

Estimates of the inertia and magnetic tensors are made similar to those of certain actual rocket bodies:

$$\mathbf{J} = \begin{bmatrix} 10739 & 0 & 0 \\ 0 & 10815 & 0 \\ 0 & 0 & 1441 \end{bmatrix} \text{ kg m}^2, \quad \mathbf{S} = \begin{bmatrix} 2.18 & 0 & 0 \\ 0 & 2.18 & 0 \\ 0 & 0 & 1.32 \end{bmatrix} \times 10^6 \text{ S m}^4. \quad (4)$$

Here, both tensors are written in the body-fixed reference frame. The magnetic tensor \mathbf{S} is assumed to be diagonal with two equal components corresponding to axes perpendicular to the rocket-body symmetry axis. The inertia tensor does have a slight asymmetry, which is neglected for simplicity in the analytical study. Thus, in Sect. 3 the inertia tensor is assumed to have a form

$$\mathbf{J} = \text{diag}(A, A, C), \quad A > C. \quad (5)$$

The magnetic tensor of the form (4) can be represented as

$$\mathbf{S} = S_* \text{diag}(1, 1, \lambda), \quad (6)$$

where the coefficient λ shows the difference of the tensor from a spherical one.

Let us emphasize that the axial symmetry approximation, which is made in (5)–(6), is not at all restrictive: the subsequent analysis involves averaging both inertia and magnetic tensors over a period of object's rotation about the axis with the greatest moment of inertia. After such averaging, an arbitrary tensor is not different from axially symmetric. In general case, for an object with principal moments of inertia $J_{x'x'}, J_{y'y'}, J_{z'z'} (J_{y'y'} \geq J_{x'x'} \geq J_{z'z'})$, $J_{y'y'} > J_{z'z'}$) and magnetic tensor with diagonal components $S_{x'x'}, S_{y'y'}, S_{z'z'}$ written in the same axes (magnetic tensor here does not have to be diagonal) the “effective” values of A , C , S_* , and λ can be calculated as follows:

$$\begin{aligned} A &= J_{y'y'}, \quad C = J_{z'z'} + J_{x'x'} - J_{y'y'}, \\ S_* &= S_{y'y'}, \quad \lambda = \frac{S_{z'z'} + S_{x'x'}}{S_{y'y'}} - 1. \end{aligned} \quad (7)$$

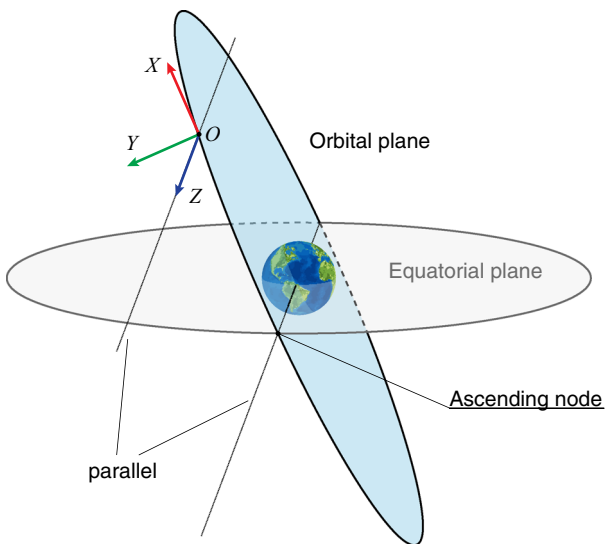
No other modifications in any subsequent formulae are required.

Using the presented set of parameters, one can estimate the characteristic values of the gravity-gradient (2) and the eddy-current (3) torques:

$$\begin{aligned} M_G &\sim 2.6 \text{ mN m}, \\ M_{EC} &\sim 0.17 \text{ mN m}. \end{aligned} \quad (8)$$

The fact that $M_{EC} \ll M_G$ allows us to place these torques to the different levels of the perturbation hierarchy.

Fig. 1 Semi-orbital reference frame



3 Analytical study of fast rotations evolution

We shall start examining the secular effects in the attitude dynamics of space debris with the analysis of fast rotations evolution. This analysis, as we have mentioned in the Introduction, is carried out in two steps. At first, we discuss the influence of the dominant conservative disturbances (gravity-gradient torques and orbit precession). Secular effects caused by these disturbances are well known to specialists; nevertheless, we begin by briefly reviewing these effects to pave the way for the next step of our analysis. Since the non-conservative perturbation (eddy-current torque) is weaker than the conservative one [see estimates (8)], we find it possible to take the “conservative” model as a point of departure for studying the “non-conservative” evolution by perturbation techniques.

3.1 Reference frames

We shall use several reference frames with the common origin in the object’s center of mass O .

$OXYZ$ is a semi-orbital reference frame: axis OY is perpendicular to the orbital plane, axis OZ is parallel to the vector from the Earth’s center to the ascending node, and axis OX completes the right-handed coordinate system (Fig. 1).

$Oxyz$ is a reference frame bound to the angular momentum \mathbf{L} of the object with respect to its center of mass: axis Oy goes along \mathbf{L} , and axis Ox lies in the orbital plane (Fig. 2). The attitude of $Oxyz$ with respect to $OXYZ$ is described by angles ρ, σ . (Let us note that given the values of these angles, we define the direction of the angular momentum \mathbf{L} as well.)

$O'x'y'z'$ is a body-fixed frame with the axes directed along the object’s principal axes of inertia. This is the frame in which tensors \mathbf{J} and \mathbf{S} in (4)–(7) are written.

Numeric experiments show that the flat rotation regime, which sets in after the transient stage, is preserved during the subsequent stage of exponential deceleration. That is to say, vector \mathbf{L} remains virtually perpendicular to the object’s symmetry axis. This fact helps simplifying the mathematical model: we further assume that Oy' is always directed along \mathbf{L} and

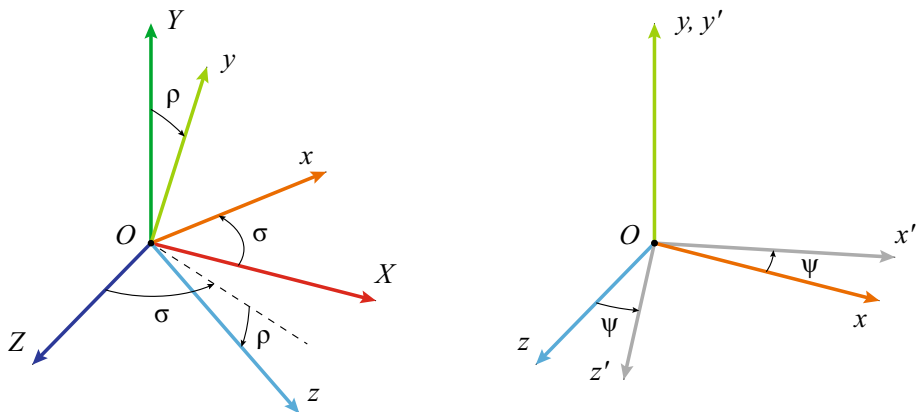


Fig. 2 Orientation of reference frame $Oxyz$ relative to $OXYZ$ (left) and orientation of reference frame $Ox'y'z'$ relative to $Oxyz$ (right)

thus coincides with Oy . (This approach allows rigorous justification, which is omitted here.) Let ψ be a rotation angle around Oy , which describes the attitude of the body frame $Ox'y'z'$ with respect to $Oxyz$. When $\psi = 0$, the two frames coincide with each other (Fig. 2).

We shall denote the unit vectors of the introduced reference frames by e_ξ , where the lower index ξ refers to the corresponding coordinate axis $\xi \in \{X, \dots, x, \dots, x', \dots\}$. The unit vector e_y can also be denoted by e_L to emphasize that it is directed along \mathbf{L} .

Let us introduce two transformation matrices:

$$\boldsymbol{\Gamma} = \begin{bmatrix} \cos \sigma & 0 & -\sin \sigma \\ \sin \sigma \sin \rho & \cos \rho & \cos \sigma \sin \rho \\ \sin \sigma \cos \rho & -\sin \rho & \cos \sigma \cos \rho \end{bmatrix}, \quad \boldsymbol{\Gamma}' = \begin{bmatrix} \cos \psi & 0 & -\sin \psi \\ 0 & 1 & 0 \\ \sin \psi & 0 & \cos \psi \end{bmatrix},$$

where $\boldsymbol{\Gamma}$ transforms vectors from semi-orbital reference frame to $Oxyz$, and $\boldsymbol{\Gamma}'$ transforms vectors from $Oxyz$ to the body frame $Ox'y'z'$.

3.2 “Conservative” evolution ($\mathbf{M}_{EC} = 0$)

The combined influence of the gravity-gradient torque and the orbit evolution on the rotational motion of a satellite was studied in Cochran (1972) and Henrard and Murigande (1987). In this case, the magnitude of the angular momentum vector is an approximate integral of motion. The direction of \mathbf{L} with respect to the semi-orbital frame is described by the equations:

$$\frac{d\sigma}{d\tau} = \frac{\partial \mathcal{H}}{\partial p}, \quad \frac{dp}{d\tau} = -\frac{\partial \mathcal{H}}{\partial \sigma}, \quad (9)$$

where

$$\begin{aligned} \mathcal{H} &= -\sqrt{1-p^2} \sin \sigma \sin i - p \cos i - \frac{\kappa_i p^2}{2\omega}, \\ p &= \cos \rho, \quad \omega = \frac{|\mathbf{L}|}{A\omega_*}, \quad \omega_* = \frac{3}{4} \left(1 - \frac{C}{A}\right) \frac{\omega_o^2}{n_\Omega \kappa_i}, \\ \kappa_i &= (\cos^{2/3} i + \sin^{2/3} i)^{3/2}, \quad \tau = n_\Omega t. \end{aligned} \quad (10)$$

The idea of how to obtain the “conservative” evolution equations (9) is given, for example, in the paper Fabrycky et al. (2007). To simplify further application of perturbation techniques, Formulae (9)–(10) are written in terms of dimensionless variables and parameters. (For instance, τ is the dimensionless time.)

It is important to note that system (9) admits stationary solutions, which are referred to as *Cassini states* (Henrard and Murigande 1987). The number of the Cassini states can be either four or two, depending on whether the object’s angular velocity value is greater than the auxiliary quantity ω_* introduced by (10). Thus, the dimensionless angular velocity ω in (10) is defined in such a way that the bifurcation is reached at $\omega = 1$. For typical rocket bodies in SSO, the bifurcation value ω_* of angular velocity is about $100^\circ/s$, which is significantly greater than the observed angular velocities immediately after payload separation. Therefore, without loss of generality, we shall further consider only $\omega < 1$, in which case there are always four Cassini states: three stable and one unstable (Henrard and Murigande 1987).

If we draw trajectories of the unit vector

$$\mathbf{e}_L = \left(\sqrt{1-p^2} \sin \sigma, p, \sqrt{1-p^2} \cos \sigma \right)^T$$

on the surface of a sphere S^2 , the separatrices proceeding out of the unstable equilibrium divide this surface into three regions (Fig. 3). Depending on positions of these regions with respect to the orbital plane, we shall denote them by R_U (upper), R_M (middle), and R_L (lower). The stable Cassini states belonging to these regions are denoted by P_U , P_M , and P_L , respectively. The unstable Cassini state is denoted by P_S . The values of p in the Cassini states are roots of the equation:

$$p^4 + 2\left(\frac{\omega}{\kappa_i}\right) \cos i \cdot p^3 + \left[\left(\frac{\omega}{\kappa_i}\right)^2 - 1\right] \cdot p^2 - 2\left(\frac{\omega}{\kappa_i}\right) \cos i \cdot p - \left(\frac{\omega}{\kappa_i}\right)^2 \cos^2 i = 0. \quad (11)$$

For nearly polar retrograde orbits, approximate expressions for the roots of Eq. (11) can be easily obtained as:

$$\begin{aligned} P_U \text{ state: } p &= (1 - \omega^2)^{1/2} + O(\cos i), \quad \sigma = \frac{\pi}{2}; \\ P_S \text{ state: } p &= \frac{\cos i}{1 - \omega} + O(\cos^2 i), \quad \sigma = \frac{\pi}{2}; \\ P_M \text{ state: } p &= -\frac{\cos i}{1 + \omega} + O(\cos^2 i), \quad \sigma = \frac{3\pi}{2}; \\ P_L \text{ state: } p &= -(1 - \omega^2)^{1/2} + O(\cos i), \quad \sigma = \frac{\pi}{2}. \end{aligned}$$

Let us use the value h of the Hamiltonian \mathcal{H} along the corresponding solution and the value of the dimensionless angular velocity ω as parameters in the family of periodic solutions to the system given by Eq. (9):

$$\sigma(\tau, h, \omega), \quad p(\tau, h, \omega). \quad (12)$$

We shall refer to these periodic solutions as *Cassini cycles*. They are represented by closed curves on the sphere S^2 around the stable Cassini states (Fig. 3).

Let us consider the values that the Hamiltonian $h(\omega)$ can take on the solutions (12). The maximum $h_M(\omega)$ and the minimum $h_L(\omega)$ values of the Hamiltonian correspond to the stationary solutions P_M and P_L , respectively. In the region R_U , the minimum of the Hamiltonian $h_U(\omega)$ is reached on the stationary solution P_U . Separatrices have the same value of the Hamiltonian $h = h_S(\omega)$ with the unstable stationary solution P_S . It follows

Fig. 3 Cassini states and Cassini cycles

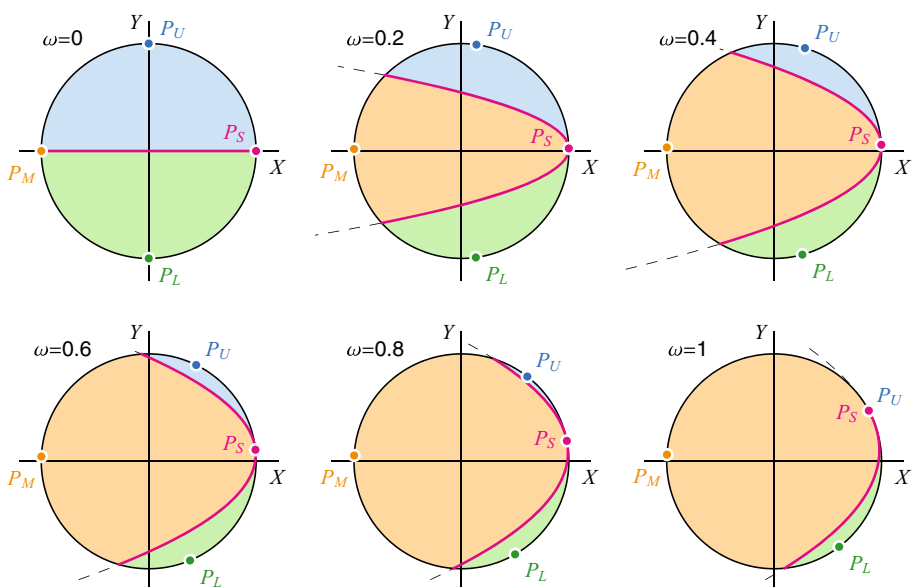
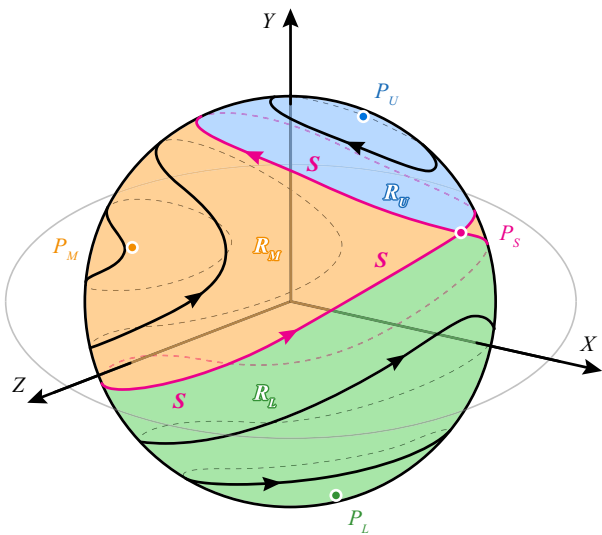


Fig. 4 Cassini cycles and separatrices dividing the regions R_U , R_M , and R_L for different values of dimensionless angular velocity ω . Cases $\omega = 0$ and $\omega = 1$ are degenerate. Bifurcation takes place for $\omega = 1$: Cassini states P_U and P_S merge, and R_U region vanishes. For $\omega \rightarrow 0$ (i.e., for very slow rotations), the width of R_M region tends to zero

that for the trajectories enclosing P_M (i.e., trajectories belonging to R_M): $h \in (h_S, h_M)$, for trajectories in R_U : $h \in (h_U, h_S)$, and for trajectories in R_L : $h \in (h_L, h_S)$. Transformations of the regions R_M , R_U , and R_L for different values of ω are shown in Fig. 4.

Vector \mathbf{L} moves along a Cassini cycle with a period, which is calculated as follows

$$T_{\text{Cassini}}(h, \omega) = 2 \int_{p_{\min}}^{p_{\max}} \frac{dp}{(dp/d\tau)} = 2 \int_{p_{\min}}^{p_{\max}} \frac{dp}{\sqrt{R_4(p)}} = \frac{4\omega}{\kappa_i} I_0. \quad (13)$$

Here, p^{\max} and p_{\min} are maximum and minimum values of p for a given cycle, respectively, and designation I_k is used for integrals

$$I_k = \int_{p_{\min}}^{p_{\max}} \frac{p^k dp}{\sqrt{-(p - p_1)(p - p_2)(p - p_3)(p - p_4)}}, \quad (14)$$

where p_1, \dots, p_4 are roots of the equation $R_4(p) = 0$,

$$R_4(p) = (1 - p^2) \sin^2 i - \left(h + p \cos i + \frac{\kappa_i p^2}{2\omega} \right)^2. \quad (15)$$

For values of $h \in (h_U, h_S)$, which correspond to Cassini cycles in R_L or R_U , roots $p_1, \dots, p_4 \in \mathbb{R}^1$; for $h < h_U$ (Cassini cycle in R_L) or $h > h_S$ (Cassini cycle in R_M) roots $p_1, p_2 \in \mathbb{R}^1, p_3, p_4 \in \mathbb{C}^1$ ($p_4 = \bar{p}_3$). The values of integration limits in (13) for cycles in R_L and R_M are $p_{\min} = p_1, p^{\max} = p_2$; the corresponding values for cycles in R_U are $p_{\min} = p_3, p^{\max} = p_4$. (Rational roots of Eq. (15) are arranged in ascending order of magnitude.)

Integrals I_k can be expressed through complete elliptic integrals of 1st, 2nd, and 3rd kind (Byrd et Friedman 1954).

3.3 Derivation of evolution equations describing the eddy-current torque impact: averaging along the orbital motion and rotation about the center of mass

Let us introduce the dimensionless eddy-current torque:

$$\mathbf{m}_{EC} = (B_*^2 S_* \omega_*)^{-1} \mathbf{M}_{EC}, \quad (16)$$

where $B_* = \mu_0 \mu_E / (4\pi R_O^3)$ is the characteristic magnitude of the magnetic field along the orbit, and S_* is the characteristic value of the magnetic tensor, which was previously defined by (6). Let us denote by $\mathcal{B} = \mathbf{B}/B_*$ the dimensionless vector of the magnetic field, whose components in the semi-orbital frame can be expressed in terms of inclination i and the argument of latitude u :

$$\mathcal{B}_X = (1 - 3 \sin^2 u) \sin i, \quad \mathcal{B}_Y = \cos i, \quad \mathcal{B}_Z = -3 \sin u \cos u \sin i.$$

To describe the evolution of rotation accounting for the influence of eddy currents, we introduce a small non-conservative perturbation associated with \mathbf{m}_{EC} into the system of equations (9):

$$\frac{d\sigma}{d\tau} = \frac{\partial \mathcal{H}}{\partial p} + \varepsilon f_\sigma, \quad \frac{dp}{d\tau} = -\frac{\partial \mathcal{H}}{\partial \sigma} + \varepsilon f_p, \quad \frac{d\omega}{d\tau} = \varepsilon f_\omega, \quad (17)$$

where

$$\begin{aligned}\varepsilon &= \frac{B_*^2 S_*}{An_\Omega}, \quad f_\sigma = \frac{1}{\omega\sqrt{1-p^2}} (\mathbf{e}_x, \langle m_{EC} \rangle_{\psi,u}), \\ f_p &= -\frac{1}{\omega} \sqrt{1-p^2} (\mathbf{e}_z, \langle m_{EC} \rangle_{\psi,u}), \quad f_\omega = (\mathbf{e}_L, \langle m_{EC} \rangle_{\psi,u}), \\ \langle \cdot \rangle_{\psi,u} &= \frac{1}{4\pi^2} \iint (\cdot) d\psi du.\end{aligned}$$

Relations (17) can be obtained by a reduction to the case of flat rotation of more general evolution equations, proposed by Beletsky in his classical studies on attitude dynamics (Beletsky 1966).

To study the secular effects in the attitude motion with the use of Eq. (17), we need to obtain an expression for the averaged dimensionless torque $\langle m_{EC} \rangle_{\psi,u}$. For convenience, we shall represent the m_{EC} as the sum of two terms, which will be averaged separately:

$$m_{EC} = m_{EC,1} + m_{EC,2}. \quad (18)$$

The term

$$m_{EC,1} = \mathcal{B} \times \Sigma (\mathcal{B} \times \omega \mathbf{e}_L) \quad (19)$$

may be called a *dissipative component*, as it causes the slowing down of the object's rotation (Ormsby 1967). Here, Σ is the dimensionless magnetic tensor obtained by transforming tensor $\Sigma' = \mathbf{S}/S_* = \text{diag}(1, 1, \lambda)$ from the body-fixed frame $Ox'y'z'$ to OXZ . The second term in (18) will be called an *orbital component*, as it is related to the change of the magnetic field along the orbit [term **B** in (3)]:

$$m_{EC,2} = \chi \mathcal{B} \times \Sigma \frac{d\mathcal{B}}{du} = -\chi \mathcal{B} \times \Sigma (2\mathcal{B} \times \mathbf{e}_Y + \sin i \cdot \mathbf{e}_Z), \quad \chi = \frac{\omega_D}{\omega_*}, \quad (20)$$

where ω_D and ω_* were previously introduced in (1) and (10).

Remark It follows from $\omega_D \ll \omega_*$ that $\chi \ll 1$ and $|m_{EC,1}| \gg |m_{EC,2}|$ at the stage of exponential deceleration ($\omega \sim 1$). Nevertheless, our numeric experiments show that if the influence of $m_{EC,2}$ is neglected, there appears a significant discrepancy between the solutions of non-averaged equations and solutions of the system (17), which arises long before the moment when the angular velocity value becomes comparable to $\omega_D \approx \omega_o$.

Let us start the averaging procedure with the first term of m_{EC} . Introducing for vector \mathcal{B} the matrix

$$\hat{\mathcal{B}} = \begin{bmatrix} 0 & -\mathcal{B}_Z & \mathcal{B}_Y \\ \mathcal{B}_Z & 0 & -\mathcal{B}_X \\ -\mathcal{B}_Y & \mathcal{B}_X & 0 \end{bmatrix},$$

we shall transform the expression for $m_{EC,1}$ as follows:

$$m_{EC,1} = \omega \hat{\mathcal{B}} \Sigma \hat{\mathcal{B}} \mathbf{e}_L = \omega \hat{\mathcal{B}} \Gamma^T \Gamma'^T \Sigma' \Gamma' \Gamma \hat{\mathcal{B}} \mathbf{e}_L. \quad (21)$$

Considering that the components of the magnetic field vector are written in the semi-orbital reference frame, we average the expression (21) over ψ :

$$\langle m_{EC,1} \rangle_\psi = \omega \hat{\mathcal{B}} \langle \Sigma \rangle_\psi \hat{\mathcal{B}} \mathbf{e}_L,$$

where

$$\langle \Sigma \rangle_\psi = \Gamma^T \langle \Sigma'' \rangle_\psi \Gamma, \quad \langle \Sigma'' \rangle_\psi = \langle \Gamma'^T \Sigma' \Gamma' \rangle_\psi = \begin{bmatrix} \frac{1+\lambda}{2} & 0 & 0 \\ 0 & 1 & 0 \\ 0 & 0 & \frac{1+\lambda}{2} \end{bmatrix}.$$

Taking into account

$$\Gamma^T \langle \Sigma'' \rangle_\psi \Gamma = \frac{1+\lambda}{2} \mathbf{E}_3 + \frac{1-\lambda}{2} \mathbf{e}_L \mathbf{e}_L^T,$$

where \mathbf{E}_3 is the identity matrix, we obtain the following expression for $\langle m_{EC,1} \rangle_\psi$:

$$\langle m_{EC,1} \rangle_\psi = \frac{(1+\lambda)\omega}{2} \hat{\mathcal{B}}^2 \mathbf{e}_L. \quad (22)$$

Averaging of Eq. (22) along the orbital motion yields:

$$\langle m_{EC,1} \rangle_{\psi,u} = -\frac{(1+\lambda)\omega}{2} \Xi \mathbf{e}_L, \quad (23)$$

where

$$\Xi = \begin{bmatrix} \xi_{11} & \xi_{12} & 0 \\ \xi_{21} & \xi_{22} & 0 \\ 0 & 0 & \xi_{33} \end{bmatrix},$$

$$\xi_{11} = 1 + \frac{1}{8} \sin^2 i, \quad \xi_{12} = \xi_{21} = \frac{1}{4} \sin 2i,$$

$$\xi_{22} = \frac{5}{2} \sin^2 i, \quad \xi_{33} = 1 + \frac{3}{8} \sin^2 i.$$

If $\sin i \neq 0$, the matrix Ξ is positive definite. The greatest and the smallest eigenvalues of this matrix are

$$\eta_{\min,\max} = \frac{1}{2} \left(1 + \frac{21}{8} \sin^2 i \pm \sqrt{1 - \frac{15}{4} \sin^2 i + \frac{297}{64} \sin^4 i} \right).$$

Let us proceed to the averaging of the second (orbital) term of the m_{EC} torque. In the expression for $m_{EC,2}$, we shall also replace the dimensionless vector \mathcal{B} by the matrix $\hat{\mathcal{B}}$:

$$m_{EC,2} = -\chi \left[2\hat{\mathcal{B}} \Sigma \hat{\mathcal{B}} \mathbf{e}_Y + \sin i \cdot \hat{\mathcal{B}} \Sigma \mathbf{e}_Z \right]. \quad (24)$$

Averaging of (24) yields:

$$\langle m_{EC,2} \rangle_{\psi,u} = -\chi \left[2 \langle \hat{\mathcal{B}} \langle \Sigma \rangle_\psi \hat{\mathcal{B}} \rangle_u \mathbf{e}_Y + \sin i \langle \hat{\mathcal{B}} \rangle_u \langle \Sigma \rangle_\psi \mathbf{e}_Z \right].$$

The following relations are satisfied:

$$2 \langle \hat{\mathcal{B}} \langle \Sigma \rangle_\psi \hat{\mathcal{B}} \rangle_u \mathbf{e}_Y = -(1+\lambda)(\xi_{12} \mathbf{e}_X + \xi_{22} \mathbf{e}_Y) - (1-\lambda) \sin \rho [\langle \mathcal{B}_x \mathcal{B}_z \rangle_u \mathbf{e}_x - \langle \mathcal{B}_x^2 \rangle_u \mathbf{e}_z],$$

$$\langle \hat{\mathcal{B}} \rangle_u \langle \Sigma \rangle_\psi \mathbf{e}_Z = \frac{1}{2} \{ (1+\lambda) [\langle \mathcal{B}_Y \rangle_u \mathbf{e}_X - \langle \mathcal{B}_X \rangle_u \mathbf{e}_Y] + (1-\lambda) \sin \rho \cos \sigma [-\langle \mathcal{B}_z \rangle_u \mathbf{e}_x + \langle \mathcal{B}_x \rangle_u \mathbf{e}_z] \}, \quad (25)$$

where

$$\begin{aligned}\langle \mathcal{B}_X \rangle_u &= -\frac{1}{2} \sin i, \quad \langle \mathcal{B}_Y \rangle_u = \cos i, \quad \langle \mathcal{B}_x \rangle_u = -\frac{1}{2} \cos \sigma \sin i, \\ \langle \mathcal{B}_z \rangle_u &= -\frac{1}{2} \sin i \sin \sigma \cos \rho - \cos i \sin \rho, \quad \langle \mathcal{B}_x^2 \rangle_u = \frac{1}{4} \sin^2 i \left(\frac{9}{2} + \cos^2 \sigma \right), \\ \langle \mathcal{B}_x \mathcal{B}_z \rangle_u &= \frac{1}{2} \sin i \cos \sigma \left(\sin \rho \cos i + \frac{1}{2} \sin i \cos \rho \sin \sigma \right).\end{aligned}$$

Using the relations (25), we obtain:

$$\langle m_{EC,2} \rangle_{\psi,u} = \frac{9}{8} \chi \sin^2 i [2(1+\lambda)\mathbf{e}_Y + \sin \rho(\lambda-1)\mathbf{e}_z]. \quad (26)$$

System (17) is of instrumental value to us. We shall use it to construct evolution equations, describing the rotational motion of the object at long time intervals. It may be difficult to draw definite conclusions about the properties of motion directly from Eq. (17). However, it is worthwhile noticing that the last equation in the system (17) allows writing down the following inequalities, characterizing the changes in the value of the dimensionless angular velocity during the object's fast rotation (Sarychev and Sazonov 1982):

$$\exp \left[-\frac{\varepsilon \eta_{\max}(1+\lambda)(\tau - \tau_0)}{2} \right] \leq \omega(\tau) \leq \exp \left[-\frac{\varepsilon \eta_{\min}(1+\lambda)(\tau - \tau_0)}{2} \right]. \quad (27)$$

Inequalities (27) become invalid when the magnitude of the angular velocity becomes comparable to ω_o .

3.4 Averaging along Cassini cycles

For small ε , the behavior of the variables σ and p in the solutions of the system (17) can be described as a Cassini cycle with slowly changing parameters h, ω . Let us write the equations for h, ω and average them along the solutions (12):

$$\begin{aligned}\frac{dh}{d\tau} &= \frac{\varepsilon}{T_{\text{Cassini}}(h, \omega)} \int_0^{T_{\text{Cassini}}} \left[\frac{\partial \mathcal{H}}{\partial \sigma} f_\sigma(\sigma(\tau', h, \omega), p(\tau', h, \omega), \omega) \right. \\ &\quad \left. + \frac{\partial \mathcal{H}}{\partial p} f_p(\sigma(\tau', h, \omega), p(\tau', h, \omega), \omega) + \frac{\partial \mathcal{H}}{\partial \omega} f_\omega(\sigma(\tau', h, \omega), p(\tau', h, \omega), \omega) \right] d\tau', \\ \frac{d\omega}{d\tau} &= \frac{\varepsilon}{T_{\text{Cassini}}(h, \omega)} \int_0^{T_{\text{Cassini}}} f_\omega(\sigma(\tau', h, \omega), p(\tau', h, \omega), \omega) d\tau'.\end{aligned} \quad (28)$$

We shall refer to Eq. (28) as evolution equations. For convenience, let us write the right-hand sides of Eq. (28) as sums of integrals I_k , which were introduced previously by Eq. (14):

$$\frac{dh}{d\tau} = \frac{\varepsilon}{2I_0} \sum_{k=0}^6 C_k I_k, \quad \frac{d\omega}{d\tau} = \frac{\varepsilon}{2I_0} \sum_{k=0}^4 W_k I_k, \quad (29)$$

where

$$\begin{aligned}
 C_k &= -(1 + \lambda)c_k^{(1)} + \frac{9}{4}\chi \sin^2 i \cdot c_k^{(2)}, \quad W_k = -(1 + \lambda)w_k^{(1)} + \frac{9}{4}\chi \sin^2 i \cdot w_k^{(2)}, \\
 c_0^{(1)} &= \frac{1}{8}h(1 + 2h^2 + 3\cos 2i), \quad c_1^{(1)} = \frac{3}{16}\cos i \left[8h \left(\frac{\kappa_i}{3\omega} + h \right) + 9\cos 2i - 1 \right], \\
 c_2^{(1)} &= \frac{9}{32\omega} [2h\omega + 3\kappa_i + (5\kappa_i + 6h\omega)\cos 2i], \quad c_3^{(1)} = \frac{\kappa_i}{4\omega^2}(\kappa_i - 3h\omega)\cos i, \\
 c_4^{(1)} &= -\frac{3\kappa_i}{16\omega^2} [h\kappa_i + 3\omega(1 + 3\cos 2i)], \quad c_5^{(1)} = -\frac{3\kappa_i^2}{4\omega^2}\cos i, \quad c_6^{(1)} = -\frac{\kappa_i^3}{16\omega^3}, \\
 c_0^{(2)} &= -\frac{3 + \lambda}{\omega}\cos i, \quad c_1^{(2)} = -\frac{3 + \lambda}{\omega^2}(\kappa_i + h\omega), \quad c_3^{(2)} = \frac{5 + 3\lambda}{2\omega^2}\kappa_i, \\
 w_0^{(1)} &= \frac{\omega}{16}(19 - 4h^2 - 3\cos 2i), \quad w_1^{(1)} = -\frac{3}{2}h\omega \cos i, \\
 w_2^{(1)} &= -\frac{1}{16}[4h\kappa_i + 9\omega(1 + 3\cos 2i)], \quad w_3^{(1)} = -\frac{3}{4}\kappa_i \cos i, \quad w_4^{(1)} = -\frac{\kappa_i^2}{16\omega}, \\
 w_1^{(2)} &= 2(1 + \lambda).
 \end{aligned}$$

Upper index in $c_k^{(i)}$, $w_k^{(i)}$ denotes the corresponding component of the eddy-current torque (18). All coefficients that are not listed here equal zero.

Applying the method of averaging in situations where the qualitative transformation of motion occurs (passage through the separatrix), we rely on the justification of the correctness of this procedure, given in Neishtadt (2017). The presence of multiple fast variables in our system is not essential.

3.5 Evolution equations and qualitative analysis of large debris objects' dynamics for fast rotations about the center of mass

For a better understanding of the rotational motion evolution, let us draw phase portraits for the system (28). In order to see how far a solution goes into one of the regions $R_L - R_U$, we shall use “relative” variables \tilde{h} instead of h :

$$\begin{aligned}
 \tilde{h} &= \frac{h - h_L(\omega)}{h_S(\omega) - h_L(\omega)} \text{ (in } R_L \text{ region),} \quad \tilde{h} = \frac{h - h_S(\omega)}{h_M(\omega) - h_S(\omega)} \text{ (in } R_M \text{ region),} \\
 \tilde{h} &= \frac{h - h_U(\omega)}{h_S(\omega) - h_U(\omega)} \text{ (in } R_U \text{ region).}
 \end{aligned} \tag{30}$$

We shall also use the auxiliary variable $\tilde{\omega}$ which shows the ratio of the object's angular velocity to the mean motion ω_o . It is related to previously used dimensionless angular velocity ω as follows:

$$\tilde{\omega} = \frac{\omega_*}{\omega_o}\omega. \tag{31}$$

Figure 5 shows the phase portraits in the space $(\tilde{\omega}, \tilde{h})$, which describe the long-term evolution of Cassini cycles. The interval of angular velocities here corresponds to the applicability range of the averaged equations (29), i.e., from angular velocities comparable to mean motion ($\tilde{\omega} \sim 1$) to critical angular velocity value, at which two Cassini states vanish ($\omega = 1$). As the real values of the angular velocity are usually much smaller than ω_* , this practically covers all possible variants of the exponential deceleration stage. Generally, trajectories of

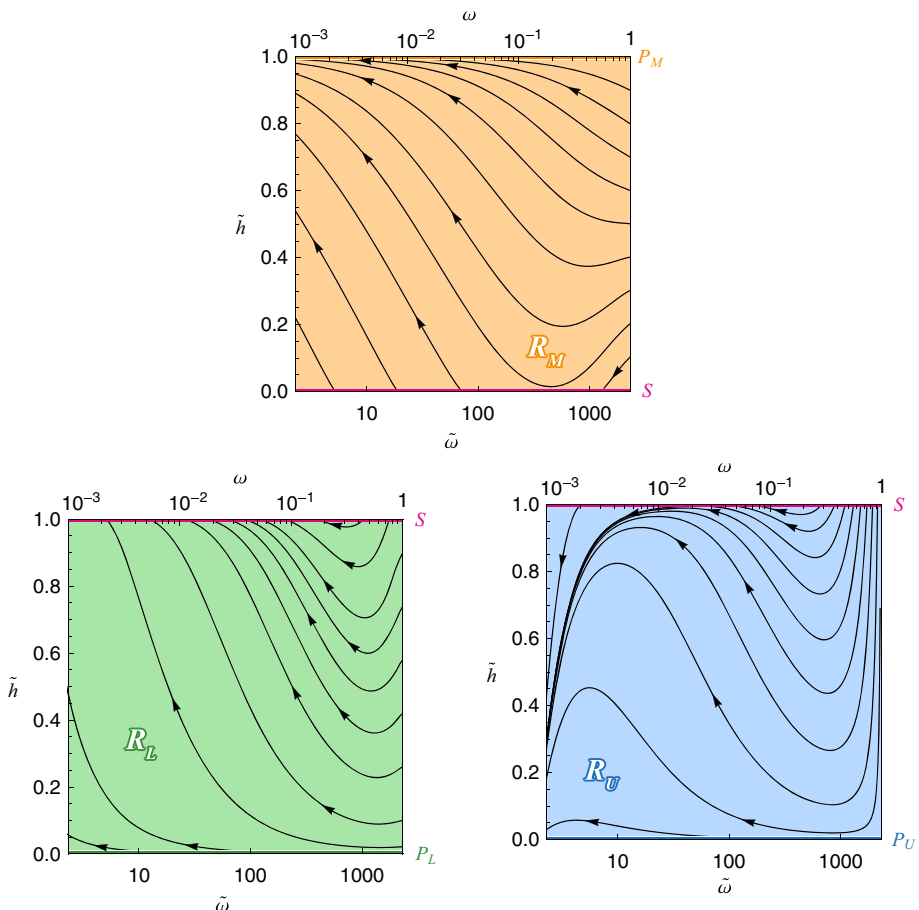


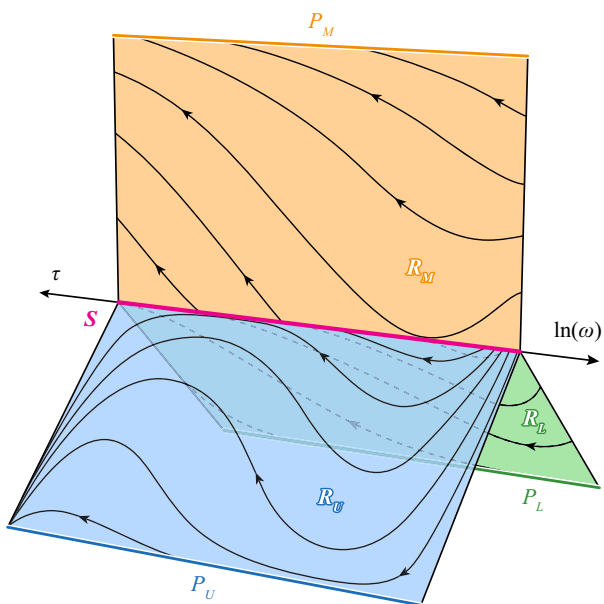
Fig. 5 Evolution of “osculating” Cassini cycles

the system depend on the object’s parameters; however, this dependence is weak and Fig. 5 correctly reflects the qualitative evolution of Cassini cycles in SSO for most objects.

Let us analyze the acquired results. Because of exponential deceleration due to eddy-current torque, all trajectories head toward the zone of lower angular velocity values (Fig. 5). A map of R_M reveals that most of the trajectories starting in this region do not leave R_M and converge toward the Cassini state P_M . The trajectories entering this region through the separatrices S also tend to P_M . Most of the trajectories in R_L are directed toward the separatrix and cross it, leaving R_L .

The dynamics in the region R_U is most interesting. Typical trajectories in this region are “S” shaped. The downward flow of trajectories in the region of high angular velocities ($\tilde{\omega} \gtrsim 700$) exists mainly as an artifact of normalization (30). Because at $\omega = 1$ the region R_U vanishes and the point P_U merges with the separatrix (Fig. 4) for $\omega \lesssim 1$, the apparent general direction of the trajectories in Fig. 6 is defined by the rapid inflation of R_U . The dynamics in the rest of the region R_U is characterized by the change in trajectories’ flow direction from upward to downward at $\tilde{\omega} \sim 10–50$. It is governed by the interplay of two components

Fig. 6 Multi-sheet phase portrait: phase portraits for regions R_U , R_M , and R_L put together



in eddy-current torque: dissipative $m_{EC,1}$ and orbital $m_{EC,2}$ given by Eqs. (19) and (20), respectively.

As $|m_{EC,1}| \propto \omega$, while $m_{EC,2}$ does not depend on ω , the evolution for very fast spins is defined by the dissipative component of the eddy-current torque, which drives the angular momentum toward the orbital plane. Consequently, for $\tilde{\omega} \in (50, 700)$ the flows of trajectories in the R_L and R_U regions are directed toward the separatrices and look very much alike.

The orbital component $m_{EC,2}$ of the eddy-current torque, as seen from Eq. (26), has a part directed along e_Y , which is close to the direction toward P_U (Fig. 4). Therefore, this component spins the debris object up about the orbital normal and results in deflection of trajectories in R_U toward P_U at $\tilde{\omega} \sim 10-50$. It should be noted that this interval corresponds to relatively fast spins for which $|m_{EC,1}| \gg |m_{EC,2}|$. However, near the separatrix the directions of these torques turn out to be such that $m_{EC,1}$ mainly affects angular velocity value, while the direction of rotational axis is primarily influenced by $m_{EC,2}$. Thus, the orbital component of eddy-current torque starts to have a noticeable effect on attitude dynamics long before the value of the angular velocity becomes comparable to mean motion.

In other words, the orbital component of the eddy-current torque keeps most of the trajectories in R_U from crossing the separatrix, while in R_L it only increases the rate at which trajectories approach the separatrix. Overall, as Fig. 5 indicates, most of the trajectories starting in R_M and R_U remain in respective regions. In contrast to this, almost all trajectories from the region R_L do cross the separatrix and transit to R_M or R_U .

To illustrate the transitions of phase trajectories between the regions, phase portraits (Fig. 5) are joined together along the separatrices, as shown in Fig. 6. Directions of transitions are indicated in Table 1.

The values $\omega_{T1} \approx 0.03$, $\omega_{T2} \approx 0.14$, $\omega_{T3} \approx 0.2$, and $\omega_{T4} \approx 0.27$ of the dimensionless angular velocity separate the attracting and repelling segments of the border S of the phase portraits in Fig. 5. Transitions in the odd columns of Table 1 have quasi-probabilistic nature (Neishtadt 2005). Roughly speaking, it means that the behavior of the original non-averaged

Table 1 Transitions between regions R_L , R_M , R_U through separatrices

$\omega < \omega_{T1}$	$\omega_{T1} < \omega < \omega_{T2}$	$\omega_{T2} < \omega < \omega_{T3}$	$\omega_{T3} < \omega < \omega_{T4}$	$\omega_{T4} < \omega < 1$
$R_L \xrightarrow{\quad R_U \quad} R_M$	$R_U \xrightarrow{\quad R_M \quad} R_L$	$R_L \xrightarrow{\quad R_U \quad} R_M$	$R_M \xrightarrow{\quad R_U \quad} R_L$	$R_M \xrightarrow{\quad R_U \quad} R_L$

system is highly sensitive to changes in the initial conditions, i.e., even small variations of phase variables may entail the change in type of the transition to follow. Therefore, uncertainties, always existing in practice, do not allow uniquely determining the type of the system's evolution near the separatrix S . Thus, it is more appropriate to discuss separatrix crossing, when two regions are available for transit, in terms of the probabilities of a trajectory going to either one of these two regions [cf. Henrard and Murigande (1987)].

3.6 Classification of long-term evolution scenarios: mapping the space of initial conditions

To study how the attitude motion evolution throughout the whole stage of exponential deceleration depends on the initial values of ρ and σ , we consider an object with parameters (4) rotating with the angular velocity $12^\circ/s$ ($\tilde{\omega} = 200$, $\omega \approx 0.086$). This value of the initial angular velocity, on the one hand, is close to angular velocity of real rocket bodies after payload separation (De Pontieu 1997) and, on the other hand, corresponds to approximately even partition of the initial conditions space to regions R_L , R_M , and R_U in terms of their area (Fig. 4), thus producing a representative set of different dynamical cases.

Let us classify different scenarios of the attitude motion long-term evolution by pairs of regions $R_i \rightarrow R_f$, where index i denotes the region in which the evolution starts, and index f indicates the region in which the system is found by the end of the exponential deceleration stage. Both indices $i, f \in \{L, M, U\}$. This notation implies nine possible scenarios. However, judging by the phase portrait of the region R_M (Fig. 5) what starts in R_M stays in R_M , and thus only one out of three $R_M \rightarrow R_f$ scenarios actually exists, namely $R_M \rightarrow R_M$. Also there are no transitions leading into R_L ; therefore, $R_U \rightarrow R_L$ is impossible as well as $R_M \rightarrow R_L$. Lastly, the scenario $R_L \rightarrow R_L$, although feasible according to Fig. 5, turns out to have a negligibly small phase area of the corresponding initial conditions. Thus, to all practical purposes there remain five different scenarios of long-term evolution:

$$R_U \rightarrow R_U, \quad R_U \rightarrow R_M, \quad R_M \rightarrow R_M, \quad R_L \rightarrow R_M, \quad R_L \rightarrow R_U.$$

To give an idea of how the phase trajectories corresponding to different scenarios are mixed, we present in Fig. 7 the partition of the initial conditions (ρ and σ) for the twice-averaged system (17).

According to the analysis in Sect. 3.5, if evolution starts in R_U , the system in most cases remains in R_U during the whole exponential deceleration stage. However, if initial conditions are close enough to separatrix, the transit $R_U \rightarrow R_M$ can take place (Fig. 6), as revealed by the narrow band between R_U and R_M corresponding to this scenario (Fig. 7).

Trajectories starting from the region R_L eventually come to the separatrix. After that they may go into R_M or R_U (Fig. 6). According to the first column of Table 1, this transition is always quasi-probabilistic at low angular velocities. Therefore, the division of long-term evolution into scenarios $R_L \rightarrow R_M$ and $R_L \rightarrow R_U$ in the lower region is quasi-probabilistic

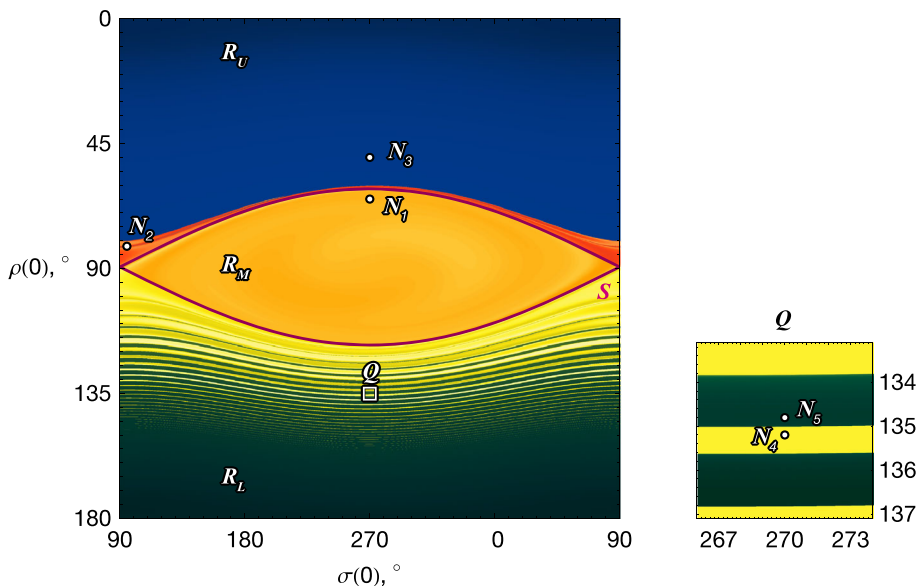


Fig. 7 Map of different evolution scenarios in the space of initial conditions for twice-averaged system. Points N_1-N_5 denote initial conditions used in numerical simulations in Sect. 4. On the right side, the enlarged sector Q of the map is shown

as well. In Fig. 7, subdomains of R_L corresponding to these two scenarios appear as tightly interleaved stripes. This clearly demonstrates the connection between quasi-probability and the high sensitivity to initial conditions: even a small variation of ρ may put the system onto a different stripe leading to a different region, which is why uncertainty in initial ρ value does not allow uniquely determining the type of subsequent evolution.

The sensitivity to initial conditions also means that the map in Fig. 7 obtained via averaged equations (17) does not predict exactly the type of evolution in the original non-averaged system. Specifically, the stripes in the lower region of this map may have a slight offset relative to their positions in the corresponding cross section of the non-averaged system's four-dimensional map. Nevertheless, Fig. 7 gives an approximately correct representation of the stripes' density and their relative widths, which define probabilities of occurrence for respective scenarios.

The actual probabilities of occurrence for scenarios $R_L \rightarrow R_M$ and $R_L \rightarrow R_U$ depend on the object's parameters: numerical experiments demonstrate that the greater relative value of the eddy-current torque results in the greater probability of transitions into R_U .

4 Numerical study of fast rotation evolution of large space debris objects in SSO

4.1 Numerical simulation setup

The regimes of motion described earlier in Sect. 3 are of temporary character. They are destroyed when the angular rate decreases to become comparable to ω_o . From this point, the rotation evolution cannot be described by Eq. (28), derived under the assumption of the

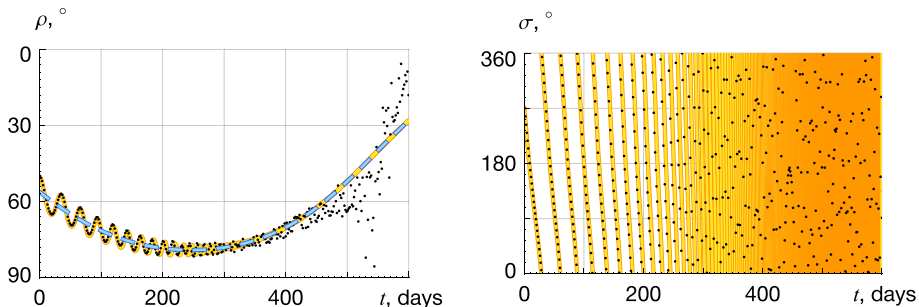


Fig. 8 Comparison of numerical simulation results (black points) with solutions of twice-averaged system (solid orange-yellow line) and thrice-averaged system (dashed cyan-blue line on $\rho(t)$ plot)

object's fast rotation. Hence, to study the transformations of the motion regimes and discover the final motion modes, we carried out numerical experiments. Furthermore, the numerical simulation was necessary to corroborate the conclusions drawn in Sect. 3 for objects with realistic parameter values (4), because in that case $\varepsilon \approx 0.5$. Yet, even for such values of the parameter ε the averaged equations (28) proved to be accurate enough to describe both qualitative and quantitative properties of the object's motion in the stage of exponential deceleration. We may also recall here that the averaging procedures were conducted with a simplified model of the magnetic field (axial dipole), whereas a more precise model (tilted dipole) is employed in simulations. The validity of this assumption is confirmed as well.

In all simulations, the following motion characteristics were kept track of:

- absolute value of angular velocity;
- angle δ between the axis with the least moment of inertia and the local vertical;
- angles ρ and σ , describing the angular momentum \mathbf{L} direction.

All simulations start from an orbital position corresponding to the crossing of the ascending node, and with the angular momentum directed along the axis with the greatest moment of inertia, i.e., flat rotation. The initial value of angular velocity equals $200\omega_0$ and is the same as in Sect. 3.6.

4.2 Simulation results: validation of the averaged equations (17) and (29)

Figure 8 shows the comparison of numerical simulation results with the solutions of twice-averaged system (17) and thrice-averaged system (29). For the latter one, we used the mean value of angle ρ in the Cassini cycle for any given h . Thrice-averaged system is not presented on $\sigma(t)$ plot, because this angle defines the position on the cycle, and this information vanishes when the motion is averaged over the cycle period. For both averaged systems, the set of parameters modified in accordance with (7) was used.

It can be seen that solution of (17), which is plotted by the orange-yellow line, closely follows the numerical results (black points) in the beginning, but then deviates from them as the time grows. This happens due to rise of fluctuations, caused by the gravity-gradient torque at smaller angular velocities. The conformity is totally lost at time $t \approx 500$ days with the end of exponential deceleration and the beginning of the chaotic stabilization stage. Angular velocity value at this moment equals approximately $4\omega_0$ (Fig. 9).

Figure 8 also demonstrates how accurately the solution of the thrice-averaged system (cyan-blue line) describes the secular evolution of the angle ρ . Figure 9 shows that plots of

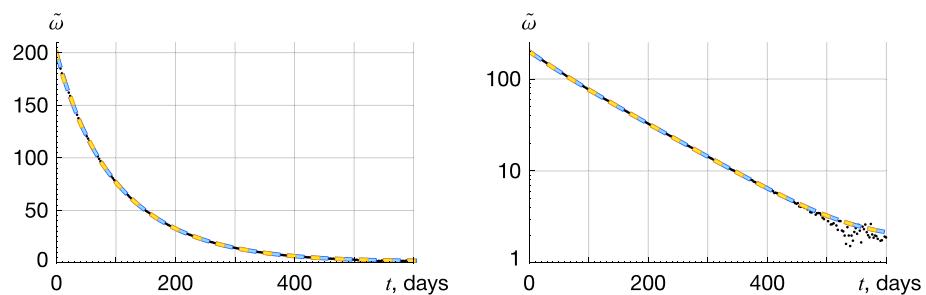


Fig. 9 Comparison of numerical simulation results (black points) with solutions of twice-averaged system (dashed orange-yellow line) and thrice-averaged system (dashed cyan-blue line) for $\tilde{\omega}(t)$ in normal (left) and semi-logarithmic (right) scales

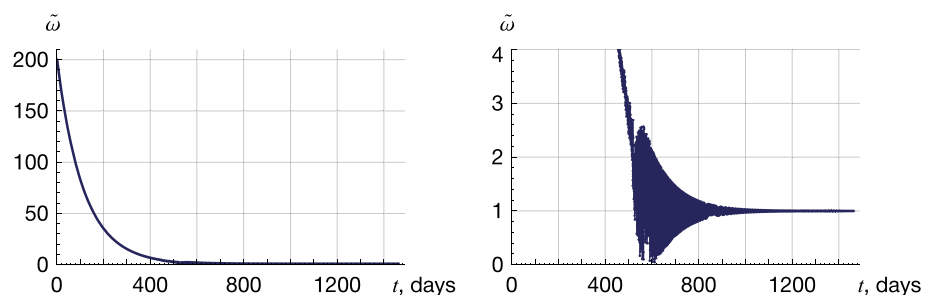


Fig. 10 Evolution of angular velocity to mean motion ratio (left), scaled fragment of evolution showing the stage of chaotic stabilization in greater detail (right)

angular velocity for twice- and thrice-averaged systems practically coincide with each other and, for times $t \lesssim 500$ days, with the results of numerical simulation.

4.3 Simulation results: exponential deceleration and chaotic stabilization

Numerical experiments show that the direction of the initial angular velocity has no significant effect on subsequent behavior of its absolute value. Typical dependence of angular velocity on time is presented in Fig. 10. It takes about 500–600 days for angular velocity to decrease to values comparable to the mean motion. The right side of Fig. 10 shows scaled graph so as to demonstrate the stage of chaotic stabilization leading to the gravity-gradient orientation of the object ($\tilde{\omega} \sim 1$).

The moment t_G when the graph $\delta(t)$ crosses the line $\delta = 90^\circ$ for the last time is natural to define as moment of gravitational capture. It is clearly seen in Fig. 11 and $t_G = 600$ – 640 days for different simulations. At $t > t_G$, angle δ converges to either 0° or 180° , as shown in Fig. 11. These outcomes are equiprobable, the only difference between them being whether the rocket body orbits the Earth with thrusters down or up. Gravitationally stabilized body rotates synchronously with the local vertical; therefore, after the $t > t_G$ the angular velocity value tends to ω_o ($\tilde{\omega} \rightarrow 1$), as seen in Fig. 10.

The invariable convergence of the evolution to the gravity-gradient orientation is a consequence of significant elongation of the considered rocket-body inertia ellipsoid, which leads to the absolutely dominant role of the gravity-gradient torque. For debris objects with less

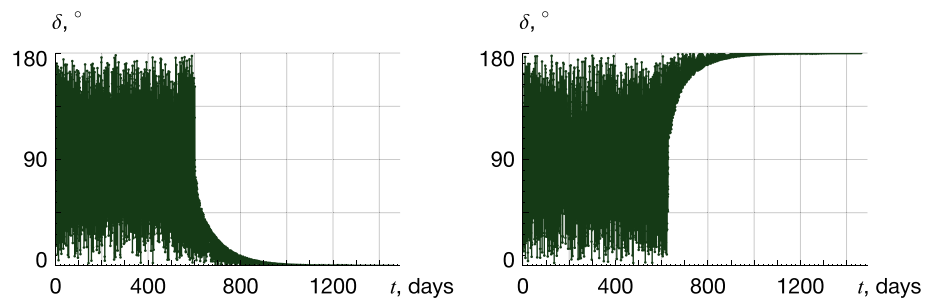


Fig. 11 Two different variants of gravity-gradient orientation

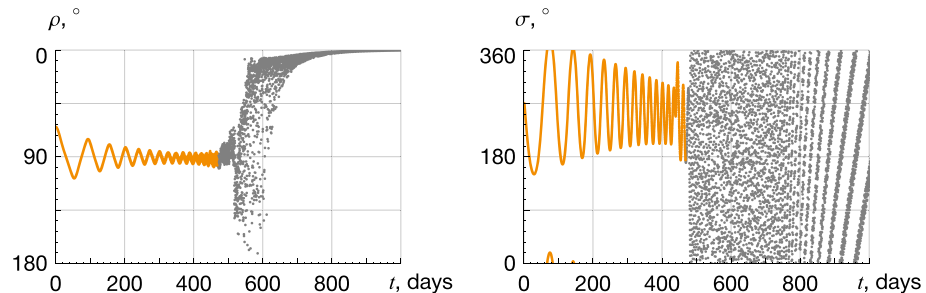


Fig. 12 Evolution of angles ρ and σ : an example of $R_M \rightarrow R_M$ scenario, based on set N_1 of initial conditions

elongated inertia ellipsoid, e.g., short rocket bodies similar to Ariane 5 or defunct satellites, other final motion regimes are possible (Efimov et al. 2017b).

4.4 Simulation results: evolution of angular momentum direction

To demonstrate all five scenarios of long-term evolution described in Sect. 3.6, numerical simulations for five sets of initial condition N_1-N_5 shown in Fig. 7 were carried out. In all subsequent plots, we shall use same colors as in Figs. 3, 4, 5 and 6 to denote different regions corresponding to the system's state during the stage of exponential deceleration: orange— R_M , blue— R_U , green— R_L . Subsequent stages of chaotic stabilization and gravity-gradient orientation are colored gray.

Figure 12 shows the evolution of angles ρ and σ in case N_1 , as an example of $R_M \rightarrow R_M$ scenario. The middle region R_M quickly becomes very narrow (Fig. 4) because ω decreases exponentially with time. Hence, motion in R_M resembles oscillations of angular momentum vector about direction $\rho \approx 90^\circ$, $\sigma \approx 270^\circ$, which for SSO approximately corresponds to the direction toward the south celestial pole. The amplitudes of these oscillations decrease over time (Fig. 12), as the system converges to Cassini state P_M (Fig. 3) in full agreement with Fig. 5.

In Fig. 13, which shows the simulation results for case N_2 , the transition from region R_U to R_M at $t \approx 140$ days is visible. As the angular momentum vector becomes captured in the middle region, the circulation of σ over the whole interval $[0^\circ, 360^\circ]$ is replaced by oscillation about $\sigma = 270^\circ$.

Convex shape of plot ρ in Fig. 14 corresponds to the concavity of trajectories in R_U in Fig. 5 at $\tilde{\omega} \sim 30$. The angle ρ increases while system comes closer to the separatrix, and

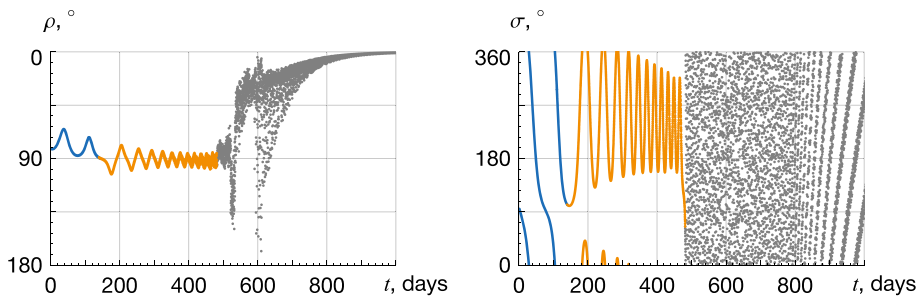


Fig. 13 Evolution of angles ρ and σ : an example of $R_U \rightarrow R_M$ scenario, based on set N_2 of initial conditions

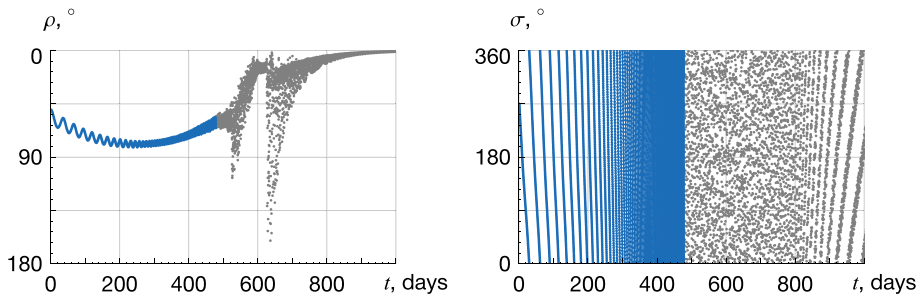


Fig. 14 Evolution of angles ρ and σ : an example of $R_U \rightarrow R_U$ scenario, based on set N_3 of initial conditions

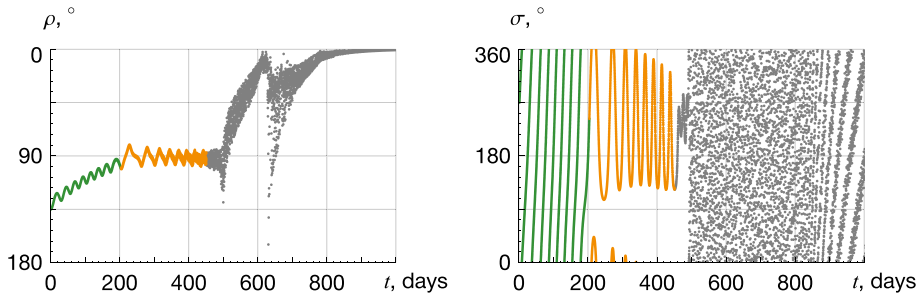


Fig. 15 Evolution of angles ρ and σ : an example of $R_L \rightarrow R_M$ scenario, based on set N_4 of initial conditions

starts to decrease, when it moves back to P_U . Thus, the axis of rotation in this scenario initially leans toward orbital plane, but deflects back to the orbital normal at $t \sim 300$ days. As explained in Sect. 3.5, this non-monotonous behavior is caused by the influence of the orbital motion on the eddy-current torque.

Evolution for case N_4 is shown in Fig. 15. Here, capture in the middle region of the trajectory that starts in R_L is seen, which is very similar to case N_2 . Alternatively, Fig. 16 shows the evolution for case N_5 that starts very close to case N_4 (Fig. 7), but instead of being captured into R_M , the system jumps past it into R_U . After that, the angular momentum vector is carried away from the orbital plane toward P_U by the orbital component of eddy-current torque, similar to the second half of the exponential deceleration stage in case N_3 .

Oscillations about the south celestial pole in R_M can also be considered as a resonance phenomenon with resonant angle σ , since in this region mean precession rate of the angular momentum vector in the inertial reference frame equals the precession rate of the orbital

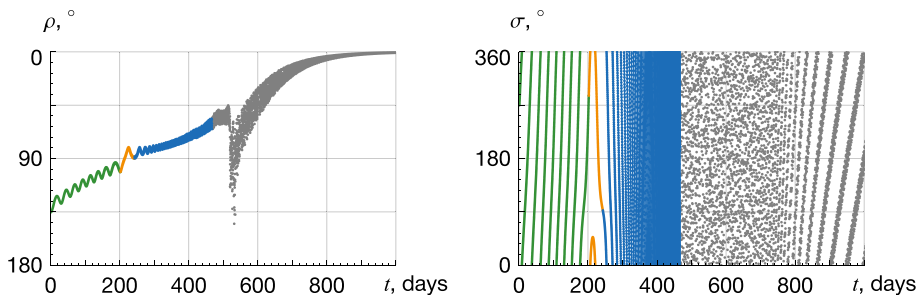


Fig. 16 Evolution of angles ρ and σ : an example of $R_L \rightarrow R_U$ scenario, based on set N_5 of initial conditions

plane ($\langle \dot{\sigma} \rangle = 0$). Then, transitions into R_M (Figs. 13, 15) correspond to the capture into resonance, while the transition $R_L \rightarrow R_U$ is passing through the resonance without capture, which is characterized by the change of resonant angle σ circulation direction (Fig. 16).

Gray parts of plots in Figs. 12, 13, 14, 15 and 16 correspond to evolution following the stage of exponential deceleration and thus complement the analytical study carried out in Sect. 3. One can see that in all cases after the end of the chaotic stabilization stage, ρ tends to 0° , as the gravitationally stabilized object rotates about the orbital normal.

5 Conclusion

Using analytical techniques and numerical simulations, we have conducted a comprehensive study of the rotational motion of large objects in SSO. It is remarkable that despite seeming insignificance, both precession of the orbit and influence of orbital motion on induced eddy currents proved to have a major impact on attitude dynamics.

The natural next step is to discover the predicted effects in the motion of the real objects. In particular, it would be desirable to check whether the angular momentum vector (for objects similar to those we have modeled) indeed oscillates in some cases about the direction to the south celestial pole.

The other potentially observable phenomenon is the lack of fast rotating objects with retrograde spins (represented by region R_L in our study). Most of them should fairly quickly switch to prograde spins or become captured into angular momentum oscillations with the axis of rotation lying near the orbital plane.

One of the possible prospects of our work is the study of the rotational evolution of large space debris objects in the satellite class. In comparison with the rocket bodies, the inertia ellipsoid of a typical satellite-like object is more similar to a sphere. Preliminary simulations show that among the final regimes for this class of objects there is not only the gravity-gradient orientation, but also rotation about the orbital plane normal with mean angular velocity equal to $9\omega_0/5$ ($\tilde{\omega} = 1.8$), which is governed by eddy currents. In addition, satellites might have a significant magnetic moment, which impacts the final stages of evolution and leads to even greater variety of final regimes, including chaotic ones (Efimov et al. 2017b; Beletsky et al. 1999).

Acknowledgements Research reported in this paper was supported by RFBR (Grant 17-01-00902).

References

- Albuja, A.A., Scheeres, D.J., McMahon, J.W.: Evolution of angular velocity for defunct satellites as a result of YORP: an initial study. *Adv. Space Res.* **56**, 237–251 (2015)
- Anselmo, L., Pardini, C.: Ranking upper stages in low Earth orbit for active removal. *Acta Astronaut.* **122**, 19–27 (2016)
- Aslanov, V., Yudintsev, V.: Dynamics of large space debris removal using tethered space tug. *Acta Astronaut.* **91**, 149–156 (2013)
- Beletsky, V.V.: Motion of an Artificial Satellite About Its Center of Mass. Israel program for scientific translations, Jerusalem (1966)
- Beletsky, V.V., Lopes, R.V.F., Pivovarov, M.L.: Chaos in spacecraft attitude motion in Earth's magnetic field. *Chaos* **9**, 493–498 (1999)
- Bonnal, C., Ruault, J.-M., Desjean, M.-C.: Active debris removal: recent progress and current trends. *Acta Astronaut.* **85**, 51–60 (2013)
- Byrd, P.F., Friedman, M.D.: *Handbook of Elliptical Integrals for Engineers and Physicists*. Springer, Berlin (1954)
- Cochran, J.E.: Effects of gravity-gradient torque on the rotational motion of a triaxial satellite in a precessing elliptic orbit. *Celest. Mech.* **6**, 127–150 (1972)
- De Pontieu, B.: Database of photometric periods of artificial satellites. *Adv. Space Res.* **19**, 229–232 (1997)
- Efimov, S., Pritykin, D., Sidorenko, V.: Attitude motion of large space debris in sun-synchronous orbits: simulation of long-term evolution. *Adv. Astronaut. Sci.* **161**, 131–142 (2017a)
- Efimov, S., Pritykin, D., Sidorenko, V.: Defunct Satellites in Nearly Polar Orbits: Long-term Evolution of Attitude Motion. [arXiv.1711.07046](https://arxiv.org/abs/1711.07046) (2017b). <https://doi.org/10.1515/astro-2018-0029>
- Fabrycky, D.C., Johnson, E.T., Goodman, J.: Cassini states with dissipation: why obliquity tides cannot inflate hot Jupiters. *Astrophys. J.* **665**, 754–766 (2007)
- Gladman, B., Dane Quinn, D., Nicholson, P., Rand, R.: Synchronous locking of tidally evolving satellites. *Icarus* **122**, 166–192 (1996)
- Golubkov, V.V.: Moment of forces in a magnetic field. *Cosm. Res.* **10**, 20–39 (1972)
- Gomez, N.O., Walker, S.J.I.: Earth's gravity gradient and eddy currents effects on the rotational dynamics of space debris objects: Envisat case study. *Adv. Space Res.* **56**, 494–508 (2015)
- Henrard, J., Murigande, C.: Colombo's top. *Celest. Mech.* **40**, 345–366 (1987)
- Hughes, P.C.: *Spacecraft Attitude Dynamics*. Dover Publications, Mineola (2004)
- International Association of Geomagnetism and Aeronomy. www.ngdc.noaa.gov/IAGA/vmod. Last checked 14 May 2018
- Koshkin, N., Korobeynikova, E., Shakun, L., Strakhova, S., Tang, Z.H.: Remote sensing of the EnviSat and Cbers-2B satellites rotation around the centre of mass by photometry. *Adv. Space Res.* **58**, 358–371 (2016)
- Kucharski, D., Kirchner, G., Koidl, F., Fan, C., Carman, R., Moore, C.: Attitude and spin period of space debris Envisat measured by satellite laser ranging. *IEEE Trans. Geosci. Remote Sens.* **52**, 7651–7657 (2014)
- Lemmens, S., Krag, H., Rosebroek, J., Carnelli, L.: Radar mappings for attitude analysis of objects in orbit. In: Proceedings of the 6th European Conference on Space Debris (2013)
- Lin, H.-Y., Zhao, C.-Y.: Evolution of the rotational motion of space debris acted upon by eddy current torque. *Astrophys. Space Sci.* **357**, 167 (2015)
- Martynenko, Y.G.: Effect of eddy currents on the rotation and attitude of a satellite. *Cosm. Res.* **23**, 347–357 (1985)
- Neishtadt, A.: Probability phenomena in perturbed dynamical systems. In: Gutkowski, W., Kowalewski, T.A. (eds.) *Mechanics of the 21st Century*. Springer, Dordrecht (2005)
- Neishtadt, A.: Averaging method for systems with separatrix crossing. *Nonlinearity* **30**(7), 2871–2917 (2017)
- Ojakangas, G.W., Anz-Meador, P., Cowardin, H.: Probable rotation states of rocket bodies in low Earth orbit. In: Proceedings of AMOS Conference (2012)
- Ormsby, J.F.A.: Eddy current torques and motion decay on rotating shells. *ESD-TR-67-94* (1967)
- Praly, N., Hillion, M., Bonnal, C., Laurent-Varin, J., Petit, N.: Study on the eddy current damping of the spin dynamics of space debris from the Ariane launcher upper stages. *Acta Astronaut.* **76**, 145–153 (2012)
- Sagnieres, L.B.M., Sharf, I.: Stochastic modeling of hypervelocity impacts in attitude propagation of space debris. *Adv. Space Res.* **59**, 1128–1143 (2017)
- Santoni, F., Cordelli, E., Piergentili, F.: Determination of disposed-upper-stage attitude motion by ground-based optical observations. *J. Spacecr. Rockets* **50**, 701–708 (2013)
- Sarychev, V.A., Sazonov, V.V.: Estimate of the influence of the dissipative magnetic moment from vortex currents on the fast rotation of a satellite. *Cosm. Res.* **20**, 297–300 (1982)

- Šilha, J., Pittet, J.-N., Hamara, M., Schildknecht, T.: Apparent rotation properties of space debris extracted from photometric measurements. *Adv. Space Res.* **61**(3), 844–861 (2018)
- Smith, G.L.: Effects of magnetically induced eddy-currents on spin motions of Earth satellite. NASA. TN-D-2198 (1964)
- Vallado, D.A.: Fundamentals of Astrodynamics and Applications. Springer, New York (2007)
- Van der Pas, N., Lousada, J., Terhes, C., Bernabeu, M., Bauer, W.: Target selection and comparison of mission design for space debris removal by DLR's advanced study group. *Acta Astronaut.* **102**, 241–248 (2014)
- Visco, M., Lucchesi, D.M.: The LArase Satellites Spin mOdel Solutions (LASSOS): a comprehensive model for the spin evolution of the LAGEOS and LARES satellites. ArXiv [arXiv:1801.09098](https://arxiv.org/abs/1801.09098) (2018)
- Ward, W.R.: Past orientation of the lunar spin axis. *Science* **183**, 377–379 (1975)
- Yanagisawa, T., Kurosaki, H.: Shape and motion estimate of LEO debris using light curves. *Adv. Space Res.* **50**, 136–145 (2012)